An Isogeometric Boundary Element Method for 3D Lifting Flows using T-splines

S.P. Chouliaras[a,*], P.D. Kaklis[a], K.V. Kostas[b], A.I. Ginnis[c], C.G. Politis[d]

[a] *Department of Naval Architecture, Ocean and Marine Engineering, University of Strathclyde, United Kingdom*
[b] *Department of Mechanical and Aerospace Engineering, Nazarbayev University, Nur-Sultan, Kazakhstan*
[c] *School of Naval Architecture and Marine Engineering, National Technical University of Athens, Greece*
[d] *Department of Naval Architecture, University of West Attica, Athens, Greece*

Abstract

In this paper an Isogeometric Boundary Element Method for three-dimensional lifting flows based on Morino's [1] formulation is presented. Analysis-suitable T-splines are used for the representation of all boundary surfaces and the unknown perturbation potential is approximated by the same T-spline basis used for the geometry. A novel numerical application of the so-called Kutta condition is introduced that utilises the advantages of isogeometric analysis with regard to the smoothness of the trailing edge curve basis functions. The method shows good agreement with existing experimental results and superior behaviour when compared to a low order panel method. The effect of the tip singularity on Kutta condition is also investigated for different levels of refinement and positions of the trailing edge collocation points.

Keywords: Isogeometric Analysis, BEM, T-splines, Lifting Flows, Potential Flow

*Corresponding author
Email addresses: sotirios.chouliaras@strath.ac.uk (S.P. Chouliaras), panagiotis.kaklis@strath.ac.uk (P.D. Kaklis), konstantinos.kostas@nu.edu.kz (K.V. Kostas), ginnis@naval.ntua.gr (A.I. Ginnis), cpolitis@uniwa.gr (C.G. Politis)

1. Introduction

Accurate and efficient calculation of the pressure distribution of lifting surfaces has been a popular topic of interest since the beginning of the 20th century in the fields of aerodynamics and hydrodynamics. Early works focused on Lifting Surface theory and an overview of methods based on this approach can be found, for example, in [2] and [3]. Numerical implementation of these methods is fast and efficient but leads to reduced accuracy due to the employed fundamental simplifications therein; with zero thickness of the lifting surface being the most critical one.

In recent times, Computational Fluid Dynamics (CFD) methods and especially the ones solving Reynolds-Averaged Navier-Stokes equations (RANS) have become the new norm in many applications. Examples of such methods are presented in [4] for wings and airfoils and [5] for ducted propellers. They offer high accuracy at the cost of increased computational resources. Furthermore, RANS methods are sensitive to the employed computational mesh, especially near the body and thus, proper mesh generation is of great importance, which can be a very time-consuming process.

Boundary Element Methods (BEM) appeared in the 60s and strike a balance between Lifting Surface theory and CFD methods. They use a boundary representation of the lifting surface that can adequately model complex geometries, e.g., propeller blades or wings with geometric discontinuities, but at the same time follow a simplified potential flow approach that is significantly faster to implement numerically, when compared to RANS.

It was the pioneering work of Hess and Smith [6] that set the groundwork of boundary element methods for potential flows by introducing the so-called panel method. They used a Boundary Integral Equation (BIE) for the unknown potential distribution on the body surface derived from Green's second identity. Later, Hess [7] extended their original method to calculate lift forces on a lifting body by adding a wake surface leaving the trailing edge of the body and a numerical implementation of the so-called *Kutta* condition. Morino in 1974 [1]

introduced a different continuous formulation based on a perturbation potential that satisfied Laplace's equation and applied his own discrete version of Kutta condition. In the years that followed Morino's formulation became the norm due to its advantages over other approaches; see [8]. However, Morino's Kutta condition did not yield accurate results in three-dimensional flows and attempts were made to enhance it by including its non-linear character as in [8] and [9] for low-order panels, and in [10] for higher-order elements. This approach became the norm in low order panel methods and also appears in modern works as in [11], [12], [13], [14] and [15]. These works focus mainly on the topic of wake alignment and the improvement of Kutta condition.

The advent of *IsoGeometric Analysis* (*IGA*) in 2005 [16] offered an alternative approach for handling commonly-found problems in finite and boundary element methods (FEM and BEM). The IGA concept is based on representing the unknown solution field with the exact same basis used for the geometric representation of the body model. This permits the use of the geometrical model as an analysis model and no approximate meshes need to be employed as it is the case in traditional FEM and BEM. Consequently, the time-consuming and error-prone meshing process can be eliminated. The additional benefits of IGA, related to the smoothness of the basis in FEM, are well known and described in [17, 18]. IGA-enhanced BEM approaches have also gained momentum in recent years with works in different fields, including hydrodynamics [19, 20, 21], structures [22], heat transfer [23], acoustics [24], etc.

IGA applications, due to the nature of the approach, require a geometric representation that is adequately flexible for both modelling and analysis. Non-Uniform Rational B-Splines (NURBS) [25] have been the CAD industry standard for decades but they are not ideal for IGA applications, as their global tensor product structure introduces unwanted redundancies and disallows local refinement; see [22]. Many alternative representations, including hierarchical splines [26], LR-Splines [27] and T-splines [28, 29], that aim to address these NURBS deficiencies, have been proposed during the last decade. An attempt to weaken the tight coupling between geometry and analysis in IGA and remedy

the issues raised by NURBS was presented in [30]. In that work, NURBS were used for the geometry and alternative, more sophisticated representations for the unknown solution field.

In this paper, unstructured analysis-suitable T-splines are used. T-splines, introduced by Sederberg et al. in [28], constitute an extension of NURBS, and the basis linear-independence requirements that guarantee analysis suitability are described in [31]. T-splines allow T-junctions in their control grids and along with the support of extraordinary vertices in their unstructured counterpart offer some considerable advantages for both geometric modelling and analysis:

- Complex geometries may be modelled via a single T-spline surface patch;
- Local refinement is possible;
- Superfluous points are significantly reduced compared to NURBS representations;
- Multi-patch NURBS surfaces can be merged into a single gap-free T-spline surface patch.

The rest of the paper is divided into 3 main sections. Section 2 describes the continuous formulation of the problem based on Morino's approach. Section 3 begins with a brief introduction to unstructured, analysis-suitable T-splines (§3.1), followed by the discrete IGA-BEM formulation and the introduction of a novel implementation of Kutta condition which leads to a nonlinear system; see §3.2 and also [32]. Numerical results of the method are presented in §4.1 and discussed in comparison with experiments and a low-order panel method. Lastly, an investigation on the behaviour of the IGA-based Kutta condition is carried out in §4.2, with special consideration on the flow near the tip of the wing.

2. Problem formulation

Let $\mathbf{O}xyz$ be a left-handed coordinate system, with its origin at the centre of a full span wing and the $y-$axis directed upwards; see, Fig. 1. We consider the

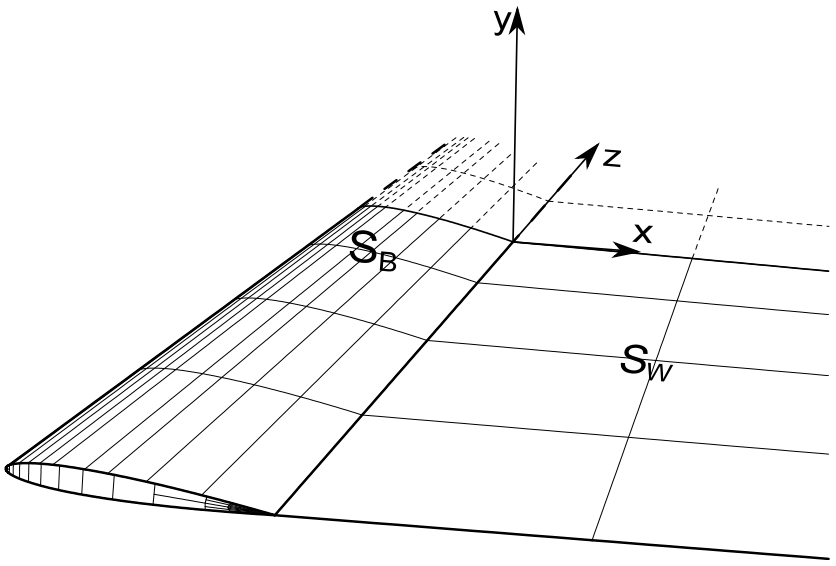

Figure 1: Boundary surfaces and coordinate system

flow of a uniform stream with velocity $\mathbf{V}_\infty$ of an ideal fluid incident on the wing. The flow, except from a free vortex sheet emanating from the trailing edge of the wing, is considered irrotational. Under these hypotheses, the flow can be described by the total potential $\Phi = \phi_\infty + \phi$ comprising the undisturbed flow potential ϕ_∞ and the perturbation potential ϕ, which represents the disturbance of the undisturbed uniform flow due to the presence of the wing. Obviously, the perturbation potential satisfies Laplace's equation:

$$\nabla^2 \phi(\mathbf{x}) = 0, \quad \mathbf{x} \in \mathcal{D}. \tag{1}$$

Here $\mathcal{D}$ denotes the open fluid domain bounded by $\partial\mathcal{D} := S = S_B \cup S_W$, where S_B denotes the boundary surface of the wing and S_W denotes the trailing vortex wake; see Fig. 1. The existence of S_W is essential for it enables the potential approach to take into account the circulation that is necessary for the existence of lifting forces on the wing [33]. In general, S_W is not known a priori and its final form is part of the problem's solution. We next proceed to provide the boundary conditions that should hold true on $\partial\mathcal{D}$.

On the wing surface S_B, the following non-penetrating boundary condition is applied

$$\frac{\partial \phi}{\partial n}(\mathbf{x}) = -\mathbf{V}_\infty \cdot \mathbf{n}(\mathbf{x}), \quad \mathbf{x} \in S_B, \tag{2}$$

where $\mathbf{V}_\infty = \nabla \phi_\infty$ is the undisturbed inflow velocity and $\mathbf{n}(\mathbf{x})$ is the outward-pointing unit normal vector of S_B.

The wake sheet is regarded as a regular surface of *discontinuity* in $\mathcal{D}$, where tangential velocity components exhibit discontinuity, although the same is not true for the normal velocity components. According to [34], the boundary conditions for the wake surface can be obtained by applying the mass and momentum conservation equations. Mass conservation yields:

$$\Delta\big(\frac{\partial \phi}{\partial n}\big) \equiv \frac{\partial \phi_u}{\partial n} - \frac{\partial \phi_l}{\partial n} = 0 \quad \text{on } S_W, \tag{3}$$

where $(\bullet)_{l,u}$ denote the lower and upper side of the wake, respectively, and $\mathbf{n}(\mathbf{x})$ is the unit normal of S_W. next, momentum conservation gives:

$$p_u - p_l = 0 \quad \text{on } S_W, \tag{4}$$

which can be further manipulated as below, using Bernoulli's equation:

$$\mid \mathbf{V_u} \mid^2 = \mid \mathbf{V_l} \mid^2 \xRightarrow{\times \frac{1}{2}} \frac{1}{2}(\mathbf{V_u} - \mathbf{V_l})\frac{1}{2}(\mathbf{V_u} + \mathbf{V_l}) = 0 \Rightarrow \mathbf{V_d} \cdot \mathbf{V_m} = 0, \tag{5}$$

i.e., $\mathbf{V_d} = \frac{1}{2}(\mathbf{V_u} - \mathbf{V_l})$ and $\mathbf{V_m} = \frac{1}{2}(\mathbf{V_u} + \mathbf{V_l})$ should be orthogonal. Condition (5) is satisfied via Kutta condition and an appropriate wake surface. In its general form, Kutta condition requires the velocity to remain bounded, i.e., $|\nabla \phi| < \infty$, at the trailing edge. Finally, the perturbation velocity must vanish at an infinite distance from the wing,

$$\nabla \phi \to 0, \quad \text{when} \quad \sqrt{x^2 + y^2 + z^2} \to \infty. \tag{6}$$

Applying Green's second identity, along with boundary conditions for the wing and the wake (Eqs. (2) and (3)), leads to the following Boundary Integral Equation (BIE):

$$2\pi\phi(\mathbf{P}) - \int_{S_B} \phi(\mathbf{Q}) \frac{\partial G(\mathbf{P},\mathbf{Q})}{\partial n(\mathbf{Q})} dS(\mathbf{Q}) - \int_{S_W} \Delta\phi(\mathbf{Q}) \frac{\partial G(\mathbf{P},\mathbf{Q})}{\partial n(\mathbf{Q})} dS(\mathbf{Q}) = \\ = \int_{S_B} V_\infty \cdot n(\mathbf{Q}) G(\mathbf{P},\mathbf{Q}) dS(\mathbf{Q}), \quad (7)$$

where $\mathbf{P}$ is permitted to lie on any smooth subset of the total boundary surface $S = S_B \cup S_W$ and $G(\mathbf{P},\mathbf{Q}) = r^{-1}(\mathbf{P},\mathbf{Q})$ is the fundamental solution of the 3D Laplace equation with $r(\mathbf{P},\mathbf{Q})$ denoting the Euclidean distance between points $\mathbf{P}$ and $\mathbf{Q}$. Furthermore, $\Delta\phi(\mathbf{Q}) = \phi_u(\mathbf{Q}) - \phi_l(\mathbf{Q})$ is the so-called potential jump with $\phi_u(\mathbf{Q})$, $\phi_l(\mathbf{Q})$ denoting the values of ϕ on the point $\mathbf{Q}$ for the upper and lower parts of the wake, respectively. It has been proven (see [35]) that the potential jump on the wake varies only along its span-wise direction and its value is determined by the value on the trailing edge, which transforms (7) as below:

$$2\pi\phi(\mathbf{P}) - \int_{S_B} \phi(\mathbf{Q}) \frac{\partial G(\mathbf{P},\mathbf{Q})}{\partial n(\mathbf{Q})} dS(\mathbf{Q}) - \int_{S_W} \Delta\phi|_{S_{W,TE}} \frac{\partial G(\mathbf{P},\mathbf{Q})}{\partial n(\mathbf{Q})} dS(\mathbf{Q}) = \\ = \int_{S_B} V_\infty \cdot n(\mathbf{Q}) G(\mathbf{P},\mathbf{Q}) dS(\mathbf{Q}), \quad (8)$$

where $\Delta\phi|_{S_{W,TE}}$ denotes the restriction of the potential jump on the wake's edge that coincides with the Trailing Edge (TE). Regarding the remaining boundary conditions, we get an automatic satisfaction of (6), while (4) is satisfied via the zero-pressure jump on the trailing edge; see also the relevant Kutta-condition discussion in §3.2.

3. An IGA-based discretisation of the Boundary Integral Equation

As mentioned in the introductory section, the IGA approach [29] is based on approximating the unknown solution field using the exact same basis functions employed for representing the geometry. This has the benefit of eliminating the geometrically inaccurate, time-consuming and error-prone process of meshing the geometrical model.

Non-Uniform Rational B-Splines (NURBS) constitute the de facto standard for representing curves and surfaces in CAD packages, however, their use has

certain drawbacks when considering the analysis phase, such as their inadequacy for local refinement; see for example [36, 37]. Based on our positive experience with employing T-splines for the surface representation and isogeometric analysis of naval hydrodynamic problems (see [36, 38, 20, 39]), this approach has been adopted for this application as well. Therefore, in this section we begin by introducing unstructured analysis-suitable T-splines and then employ them in the representation of the wing geometry as well as the approximation of the unknown quantities, namely ϕ and $\Delta\phi$, appearing in BIE (8).

3.1. Unstructured Analysis-Suitable T-splines

We focus on analysis-suitable bicubic T-spline surfaces, due to their appropriateness for engineering analysis and their support in modern CAD packages[1]. Additional information on T-splines technology, structured and unstructured T-meshes along with analysis suitability can be found in the works of Sederberg, Bazilevs and Scott; see e.g., [28, 40, 41, 29, 42, 43].

3.1.1. The unstructured T-mesh

The starting point for the definition of a T-spline surface is the T-mesh. A T-mesh consists of faces (elements), edges, and vertices of valence 4 (regular) and 3 (T-junctions); the latter depicted with black squares in Fig. 2. Unstructured T-meshes additionally support extraordinary vertices, i.e., vertices with a valence of 3, 5 and above; see for example a vertex with valence 3 depicted with a red square in Fig. 2. All elements touching an extraordinary vertex constitute its one-ring neighbourhood and similarly, the elements neighbouring this one-ring area form the two-ring neighbourhood of the same vertex, and so on. For a bicubic T-spline surface, a control point $\mathbf{d}_i, i = 0, \ldots, n_A$, is assigned to every mesh vertex, where n_A is the total number of control points/vertices.

A valid knot interval configuration must be applied on the T-mesh before the T-spline bases and surface can be defined. A non-negative knot interval value

[1]For example, Autodesk's Fusion 360 `https://www.autodesk.com/products/fusion-360/`.

is assigned on every edge of the T-mesh while making sure that knot intervals on opposite edges of the same element sum to the same value. Additionally, we assume that the assigned values for the knot intervals along the spoke edges of each extraordinary vertex are all, either zero or non-zero.

3.1.2. T-spline basis

In our work, each basis function $N_\alpha, \alpha = 1, \ldots, n_A$, is a bicubic polynomial spline defined over local knot vectors determined by the process described in [22]. The T-spline surface over each of its elements/faces e is defined as:

$$\tilde{\mathbf{x}}^{\mathbf{e}}(\tilde{\boldsymbol{\xi}}) = \sum_{\alpha=1}^{n_A} \mathbf{d}_\alpha N_\alpha^e(\tilde{\boldsymbol{\xi}}) \tag{9}$$

where $\tilde{\boldsymbol{\xi}} = (\xi, \eta)$ are the parametric coordinates for the element/face e on the T-mesh, $N_\alpha^e(\tilde{\boldsymbol{\xi}})$ is the restriction of the T-spline basis function N_α on the same parametric face and $\mathbf{d}_\alpha$ are the surface's control points

T-spline basis functions are linearly independent when the T-mesh satisfies the following topological requirements, as stated in [22]:

1. T-junction extensions should not intersect with each other;
2. no one-bay[2] face extension spans an element in the three-ring neighbourhood of an extraordinary point;
3. no extraordinary point should lie within the three-ring neighbourhood of another extraordinary point.

3.1.3. Bézier Extraction

The T-spline elements, defined in the previous section, can be decomposed into a collection of surface patches, each of them being a single bivariate polynomial, that better fits the BEM paradigm. For this purpose a Bézier extraction operator is applied which maps the global T-spline basis functions to the Bernstein

[2]The portion of a face extension lying in the face immediately adjacent to the T-junction is called a one-bay face extension.

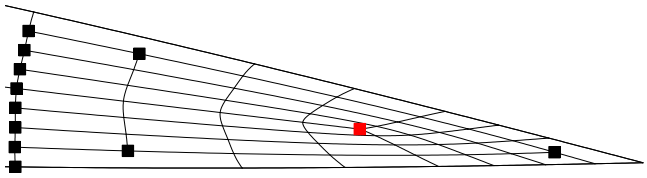

Figure 2: Example of a T-mesh part demonstrating T-junctions (black squares) and an extraordinary vertex (red square)

polynomial bases. Each T-spline basis function that is non-zero over the Bézier element e can be written as:

$$N_{\alpha}^{e}(\tilde{\boldsymbol{\xi}}) = \sum_{b=1}^{(p+1)^2} c_{\alpha,b}^{e} B_b(\tilde{\boldsymbol{\xi}}), \quad \alpha = 1, \ldots, n_e \leq n_A, \tag{10}$$

where p is the degree (in our case: $p = 3$), $B_b(\tilde{\boldsymbol{\xi}})$ are Bernstein basis polynomials of degree p, and $c_{\alpha,b}^{e}$ are the Bézier extraction coefficients. Equation (10) can also be written in matrix form:

$$\mathbf{N_e}(\tilde{\boldsymbol{\xi}}) = \mathbf{C_e}\mathbf{B}(\tilde{\boldsymbol{\xi}}),\ \mathbf{N_e} \in \mathbb{R}^{n_e}, \mathbf{C_e} \in \mathbb{R}^{n_e \times (p+1)^2},\ \mathbf{B}(\tilde{\boldsymbol{\xi}}) \in \mathbb{R}^{(p+1)^2},\ \mathbf{e} = [1, \ldots, n]. \tag{11}$$

If we further assume rational T-spline basis functions, we may express these in matrix form as follows:

$$\mathbf{R_e} = \frac{\mathbf{W_e}\mathbf{N_e}}{(\mathbf{w_e})^T\mathbf{N_e}} = \frac{\mathbf{W_e}\mathbf{C_e}\mathbf{B}(\tilde{\boldsymbol{\xi}})}{(\mathbf{w_e})^T\mathbf{C_e}\mathbf{B}(\tilde{\boldsymbol{\xi}})}, \tag{12}$$

where $\mathbf{w_e}$ is the vector of the corresponding control point weights and $\mathbf{W_e}$ is the diagonal matrix $diag(\mathbf{w_e})$. We may further note here that Bézier extraction

produces elements, i.e., Bézier elements, which are obviously represented by the same set of basis functions that is the expected behaviour of shape functions in BEM.

3.2. Isogeometric Boundary Element Method

The wing body, in our examples, assumes a multi-patch boundary representation, S_B, using m bicubic T-spline surfaces, while for the wake S_W a single bicubic T-Spline planar surface is used that is parallel to the uniform velocity as explained in [44]. Hence,

$$S_B = \bigcup_{j=1}^{m} \bigcup_{e=1}^{ne_j} S_B^{je}, \quad S_W = \bigcup_{j=1}^{1} \bigcup_{e=1}^{qe_j} S_W^{je},$$

with each of the T-spline elements $S_{[\cdot]}^{je}$, $[\cdot] \in \{B, W\}$, given by the general expression:

$$S^{je} = \tilde{\mathbf{x}}_e^j(\tilde{\boldsymbol{\xi}}) = \frac{(\mathbf{d_e}^j)^T \mathbf{W_e}^j \mathbf{C_e}^j \mathbf{B}(\tilde{\boldsymbol{\xi}})}{(\mathbf{w_e}^j)^T \mathbf{C_e}^j \mathbf{B}(\tilde{\boldsymbol{\xi}})} = (\mathbf{d_e}^j)^T \mathbf{R_e}^j(\tilde{\boldsymbol{\xi}}). \tag{13}$$

By application of the Isogeometric Analysis approach, we may express the unknown potential distribution on the wing body using the exact same basis functions employed for the geometric representation of its boundary surface. Therefore the projection of ϕ in the multi-patch T-spline space will be given by:

$$\phi(\mathbf{P}) = \sum_{i=1}^{n_j} \phi_i^j \tilde{R}_i^j(\mathbf{P}), \quad \mathbf{P} \in S_B^j,\ j = 1, \ldots, m, \tag{14}$$

where $\tilde{R}_i^j(\mathbf{P}) = R_i^{je}(\tilde{\boldsymbol{\xi}}(\mathbf{P}))$. The potential jump $\Delta\phi$ occurring at the wake is a function of the curvilinear span-wise coordinate, $s_{W,TE}$, on the trailing edge of the wing. Assuming that the trailing edge is included, in its entirety, on a single T-spline patch ($S_B^{j_{TE}}$), we can write:

$$\Delta\phi(s_{W,TE}) = \sum_{i=1}^{n_{TE}} \Delta\phi_i^{j_{TE}} R_i^{j_{TE}}(\xi_{TE}, \eta), \tag{15}$$

where the index $j_{TE} \in \{1, \ldots, m\}$ corresponds to the T-spline patch that includes the trailing edge, and n_{TE} is the number of corresponding bases with support on

the trailing edge. By collocating now the BIE (8) at $K = \sum_{j=1}^{m} n_j$ generalised Greville points (see [22]), a linear system with the same number of equations is formed:

$$
\begin{aligned}
2\pi \sum_{i=1}^{n_j} \phi_i^j \tilde{R}_i^j(\mathbf{P}_k) - \sum_{j=1}^{m} \sum_{i=1}^{n_j} \phi_i^j \int_{S_B^j} \tilde{R}_i^j(\mathbf{Q}) \frac{\partial G(\mathbf{P}_k, \mathbf{Q})}{\partial n(\mathbf{Q})} dS(\mathbf{Q}) \\
- \sum_{i=1}^{n_{TE}} \Delta\phi_i^{j_{TE}} \int_{\eta_1}^{\eta_2} R_i^{j_{TE}}(\xi_{TE}, \eta) \int_{\xi_{TE}}^{\xi_\infty} \frac{\partial G(\mathbf{P}_k, \mathbf{Q})}{\partial n(\mathbf{Q})} dS(\mathbf{Q}) \\
= \sum_{j=1}^{m} \int_{S_B^j} \mathbf{V}_\infty \cdot \mathbf{n}(\mathbf{Q}) G(\mathbf{P}_k, \mathbf{Q}) dS(\mathbf{Q}), \\
j \in \{1, \ldots, m\} : \mathbf{P}_k \in S_B^j, \quad k = 1, \ldots, K. \qquad (16)
\end{aligned}
$$

The kernel of (16) is weakly singular. Three different types of integrals are considered depending on the distance between $\mathbf{P}_k$ and $\mathbf{Q}$:

- Far field case: Let the preimage of $\mathbf{Q}$ lie on a Bézier patch $\mathbf{x}^e$ with a convex hull of its control points $conv_{\mathbf{x}^e}$. When the preimages of $\mathbf{P}_k$ and $\mathbf{Q}$ do not lie on the same element and the Euclidean distance $d(\mathbf{P}_k, conv_{\mathbf{Q}})$ between $\mathbf{P}_k$ and $conv_{\mathbf{x}^e}$ is greater than two times the diagonal of $\mathbf{x}^e$ or $d(\mathbf{P}_k, conv_{\mathbf{Q}}) > 2diag(\mathbf{x}^e)$, Gauss - Kronrod quadrature with 15 quadrature points is applied.

- Near field case: When the preimages of $\mathbf{P}_k$ and $\mathbf{Q}$ do not lie on the same element but the Euclidean distance $d(\mathbf{P}_k, conv_{\mathbf{Q}})$ between $\mathbf{P}_k$ and $conv_{\mathbf{x}^e}$ is less than two times the diagonal of $\mathbf{x}^e$ or $d(\mathbf{P}_k, conv_{\mathbf{Q}}) < 2diag(\mathbf{x}^e)$, a Telles' transformation is applied as introduced in [45] or [46], with the preimage of $\mathbf{P}_k$ regarded as the singular point of the transformation. Gauss - Kronrod quadrature with 31 quadrature points is applied on the transformed integral afterwards.

- In field case: When the preimages of $\mathbf{P}_k$ and $\mathbf{Q}$ lie on the same element the interval is partitioned into 4 sub-intervals from I to IV as demonstrated in Figure (3). Telles transformation is applied again for each sub-interval

with the preimage of $\mathbf{P}_k$ regarded as the singular point of the transformation for each of them. Gauss - Kronrod quadrature with 31 quadrature points is applied on each transformed sub-integral afterwards.

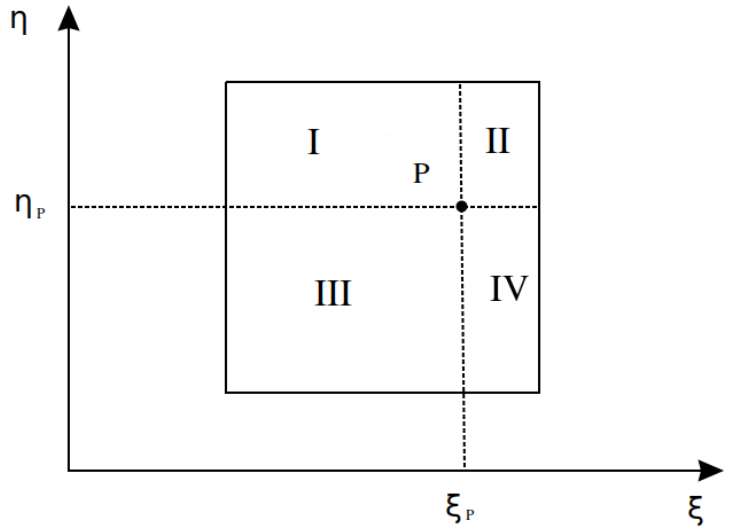

Figure 3: Interval partition for weakly singular integrals

The linear system of (16) is underdetermined, since we have K equations with $K + n_{TE}$ unknowns. The remaining equations can be obtained through the numerical application of Kutta condition which states that the fluid velocity at the trailing edge has to be finite. This definition cannot be applied directly, but, according to [7], this is equivalent to a zero pressure difference between the upper and lower parts of the trailing edge, i.e.:

$$\Delta p = p_u - p_l = \frac{1}{2}\rho \mathbf{V}_{t,u}^2 - \frac{1}{2}\rho \mathbf{V}_{t,l}^2 = 0 \tag{17}$$

where $\mathbf{V}_{t,u}$, $\mathbf{V}_{t,l}$ are the total tangential velocities on the upper and lower part of the trailing edge, respectively, and ρ is the fluid density. In IGA setting, the zero pressure jump requirement from (17) for n_{TE} collocation points distributed

on the trailing edge becomes:

$$\Delta p = \Delta p(\xi_{TE,u}, \xi_{TE,l}, \eta_k) = \frac{1}{2}\rho\Big(\mathbf{V}_{\infty,u,t} + \frac{\mathbf{e}_{1,u}}{\mid \mathbf{m}_{1,u} \mid} \sum_{i=1}^{n_{j_{TE}}} \phi_i^{j_{TE}} \frac{\partial \tilde{R}_i^{j_{TE}}(\xi_{TE,u}, \eta_k)}{\partial \xi} + \frac{\mathbf{e}_{2,u}}{\mid \mathbf{m}_{2,u} \mid \cdot sin\theta_u} \sum_{i=1}^{n_{j_{TE}}} \phi_i^{j_{TE}} \frac{\partial \tilde{R}_i^{j_{TE}}(\xi_{TE,u}, \eta_k)}{\partial \eta} - \frac{cos\theta_u \mathbf{e}_{2,u}}{\mid \mathbf{m}_{1,u} \mid sin\theta_u} \sum_{i=1}^{n_{j_{TE}}} \phi_i^{j_{TE}} \frac{\partial \tilde{R}_i^{j_{TE}}(\xi_{TE,u}, \eta_k)}{\partial \xi}\Big)^2 -$$

$$\frac{1}{2}\rho\Big(\mathbf{V}_{\infty,l,t} + \frac{\mathbf{e}_{1,l}}{\mid \mathbf{m}_{1,l} \mid} \sum_{i=1}^{n_{j_{TE}}} \phi_i^{j_{TE}} \frac{\partial \tilde{R}_i^{j_{TE}}(\xi_{TE,l}, \eta_k)}{\partial \xi} + \frac{\mathbf{e}_{2,l}}{\mid \mathbf{m}_{2,l} \mid \cdot sin\theta_l} \sum_{i=1}^{n_{j_{TE}}} \phi_i^{j_{TE}} \frac{\partial \tilde{R}_i^{j_{TE}}(\xi_{TE,l}, \eta_k)}{\partial \eta} - \frac{cos\theta_l \mathbf{e}_{2,l}}{\mid \mathbf{m}_{1,l} \mid sin\theta_l} \sum_{i=1}^{n_{j_{TE}}} \phi_i^{j_{TE}} \frac{\partial \tilde{R}_i^{j_{TE}}(\xi_{TE,l}, \eta_k)}{\partial \xi}\Big)^2 = 0, \quad k = 1, \ldots, n_{TE}. \quad (18)$$

For the various new symbols appearing in (18) some explanation is due. Firstly, $\mathbf{m}_1$, $\mathbf{m}_2$ are the linearly independent vectors tangent to the isoparametric curves on the wing, obtained by evaluating the first-order partial derivatives of the regular surface representation with respect to the parameters ξ and η, respectively and θ is the non-zero angle between them; see Fig. 4. The vectors $\mathbf{e}_1 = \mathbf{m}_1/\|\mathbf{m}_1\|$ and $\mathbf{e}_2$ correspond to a local orthonormal system derived from $\mathbf{m_1}$ and $\mathbf{m_2}$. To calculate the magnitude of the tangential velocity $\mathbf{V}_t$ of the flow at a point $\mathbf{P}$, we take the first-order partial derivatives of the velocity potential with respect to ξ and η which yield the velocity components $\mathbf{V}_{t,\xi}$ and $\mathbf{V}_{t,\eta}$ along the $\mathbf{m}_1$ and $\mathbf{m}_2$ directions, respectively. Projecting $\mathbf{V}_{t,\xi}$ and $\mathbf{V}_{t,\eta}$ on the orthonormal system $\mathbf{e}_1$ and $\mathbf{e}_2$ we can readily evaluate the magnitude of $\mathbf{V}_t$, in a similar way with the one described in [22]. Finally, the subscripts u/l denote the upper/lower part of the wing surface S_B, respectively, which is useful when dealing with a full neighborhood of TE as it is the case with (18).

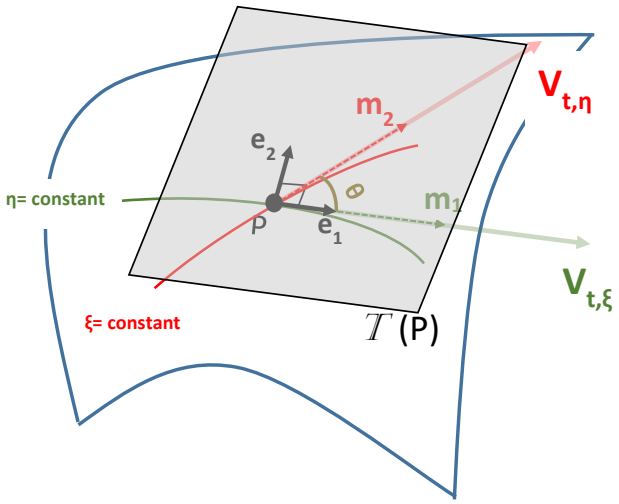

Figure 4: Velocity decomposition on the tangent plane T at a point $\mathbf{P}$ of the wing surface

Finally, the linear system (16) and the quadratic system (18) can be merged into a single non-linear system of equations as:

$$\mathcal{P}_j(\Phi) = 0, \quad j = 1, \ldots, K + n_{TE} \tag{19}$$

where Φ is the vector of all unknown coefficients:

$$\Phi = (\phi_1^1, \ldots, \phi_{n_1}^1, \phi_1^2, \ldots, \phi_{n_2}^2, \ldots, \phi_1^m, \ldots, \phi_{n_m}^m, \Delta\phi_1, \ldots, \Delta\phi_{n_{TE}})^T. \tag{20}$$

A Newton-Raphson scheme is applied for solving the non-linear system in (19):

$$\Phi^{r+1} = \Phi^r - J_r^{-1}\mathcal{P}(\Phi^r) \tag{21}$$

where J_r^{-1} is the inverse of the Jacobian matrix of (19) for step r. It is worth noting that the employed approach allows the analytic evaluation of the Jacobian matrix. This hasn't been the case in traditional panel methods where numerical schemes have been used broadly. It is only recently that an attempt was made to calculate the Jacobian analytically with an approach described in [14].

The initial approximation of the solution required by the Newton-Raphson scheme is based on Morino's Kutta condition. According to Morino [1] the

potential jump on the wake can be regarded as the difference between the potential values on the upper and lower parts of the wing on the trailing edge:

$$\Delta\phi(s_{W,TE}) = \phi(\xi_{u,TE},\eta) - \phi(\xi_{l,TE},\eta) = \sum_{i=1}^{n_{j_{TE}}} \phi_i^0 \tilde{R}_i(\xi_{u,TE},\eta) - \sum_{i=1}^{n_{j_{TE}}} \phi_i^0 \tilde{R}_i(\xi_{l,TE},\eta), \tag{22}$$

where ϕ_i^0 are the unknown potential coefficients of the zeroth iteration. Substituting (22) in the original BIE (8) and collocating again on the generalised Greville points produces a linear system whose solution is used as a first approximation of $\mathbf{\Phi}$.

4. Numerical Results

In this section, we firstly compare our IGA-based approach with a common low-order BEM method and experimental results for simple wings, and then provide a detailed numerical experimentation for the benefits stemming from the application of IGA-based Kutta condition.

4.1. Wings with constant NACA0012 airfoil section

We test the developed method in two constant-section wing cases: a rectangular unswept wing and a swept one with a 20^o sweep angle. Both wings have a semi-span of length $s = 3m$, a chord of length $c = 1m$ and are generated by translating a NACA0012 profile, represented via the parameterization described in [47]. The flow is uniform along the x-axis and the angle of attack is equal to 6.75^o. The geometric models of the wings and their respective wakes have been generated using the T-Spline plug-in for Rhinoceros 3D[3]. Views of these models are included in Fig. 5. Each model consists of the main wing (238 control points), cap (75 control points) and wake (133 control points) surfaces. This leads to a total of 320 DoFs for each example. No T-junctions or extraordinary points exist in the main wing part, and hence, these parts assume a NURBS

[3]http://www.rhino3d.com

representation. However, as can be seen by the close-up of the cap surface in Fig. 6b, T-junctions and extraordinary vertices exist there.

The pressure coefficient distributions on the pressure and suction sides of each wing are shown in Figs. 7 and 8, respectively. It is worth noting that around the tips of both wings and the mid section of the swept wing three-dimensional effects (or spanwise velocity components) emerge. The velocity vector-fields in these regions are presented in Fig. 9. Sectional chordwise pressure coefficients are calculated for each wing and compared with experimental results from [48], and simulation results from the open-source low-order panel method `xflr5`[4]. The corresponding `xlfr5` model has 3050 DoFs. Four sections for each wing are selected and shown in Fig. 10 for the unswept wing, and Fig. 11 for the swept one. Good agreement is achieved between the IGA-BEM approach and experimental results for much fewer DoFs, when compared to the low-order simulation. At the same time, the IGA-based Kutta condition shows superior accuracy on the trailing edge in comparison with `xlfr5`. This is illustrated in Fig. 12 for the mid section of the unswept wing. It is clear that the IGA-BEM method satisfies the zero pressure jump on the trailing edge while `xlfr5` doesn't. At the same time, `xlfr5` shows an oscillatory behaviour that deteriorates for higher DoFs.

Deviations between IGA-BEM and experimental results are exhibited only for sections near the wing tip, as illustrated in Fig. 10d. This occurs due to the existence of a wing tip vortex which cannot be modelled in the context of potential flow theory, as stated, for example, in [49]. A further investigation of the pressure coefficient behaviour at the tip is discussed in detail in the following subsection.

[4] http://www.xflr5.tech/xflr5.htm

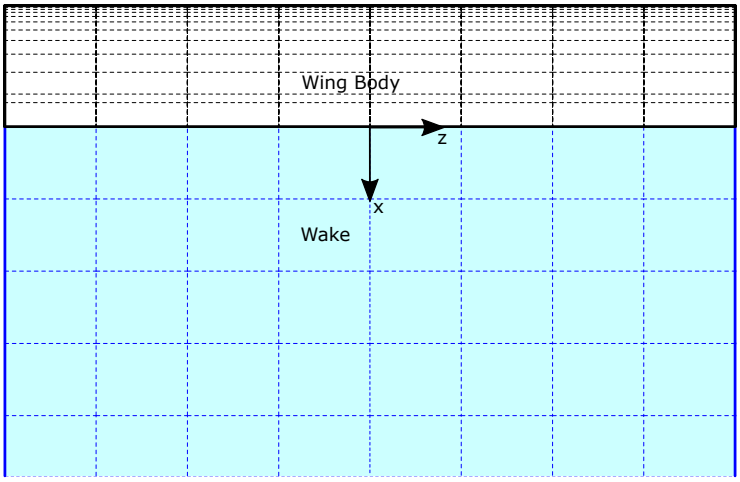

(a) Unswept

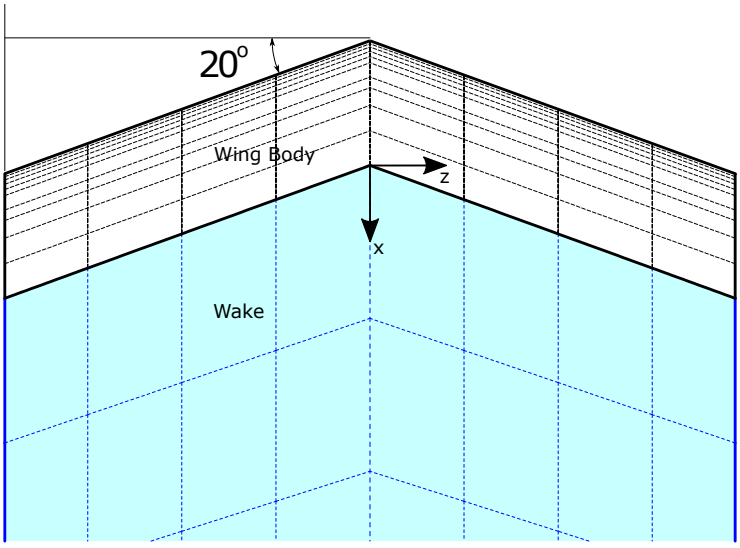

(b) Swept

Figure 5: Wing and wake surfaces of tested wings

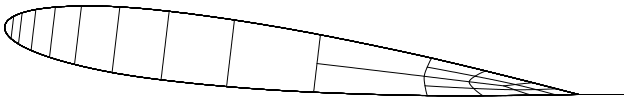

(a) Full Cap

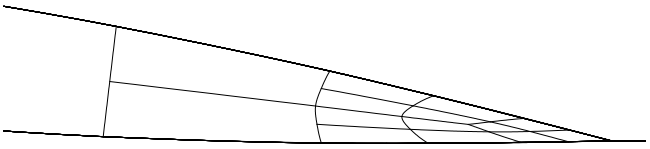

(b) T-junctions and an Extraordinary Point of valence 3 near the trailing edge

Figure 6: Wing Cap Surface

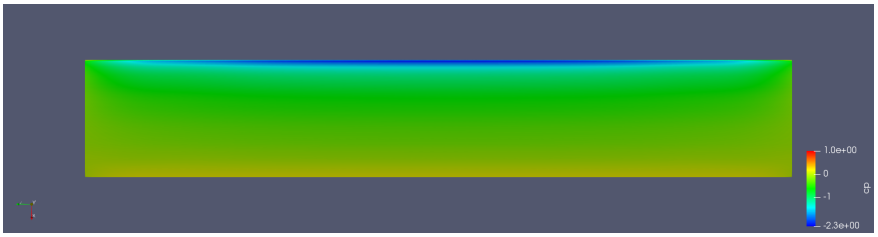

(a) Suction side

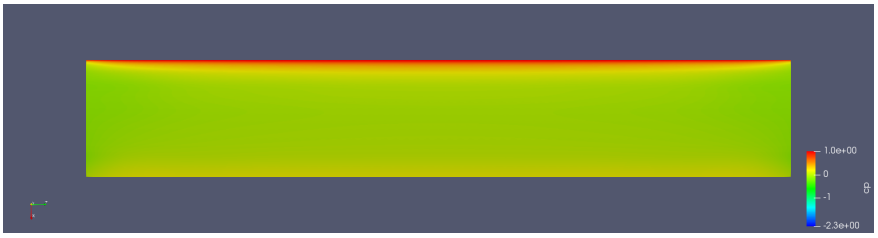

(b) Pressure side

Figure 7: Pressure coefficient distribution for an unswept wing

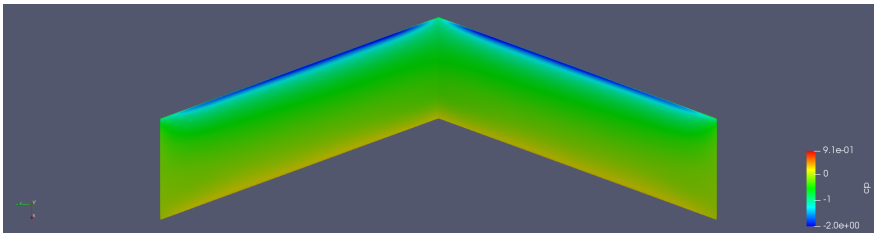

(a) Suction side

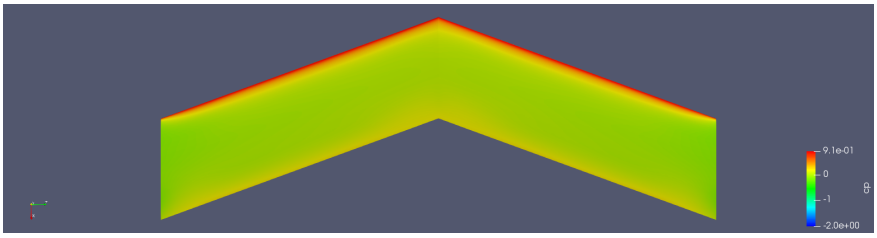

(b) Pressure side

Figure 8: Pressure coefficient distribution for a swept wing

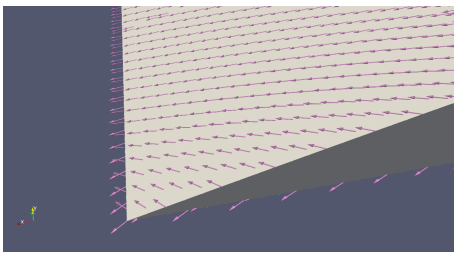

(a) Tip region of unswept wing

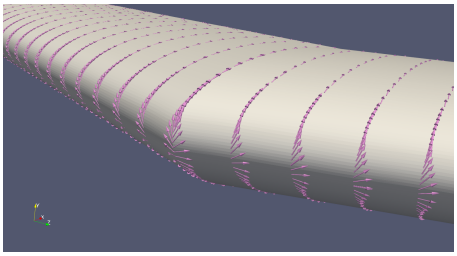

(b) Mid region of swept wing

Figure 9: Velocity vector-fields in regions where three-dimensional phenomena emerge

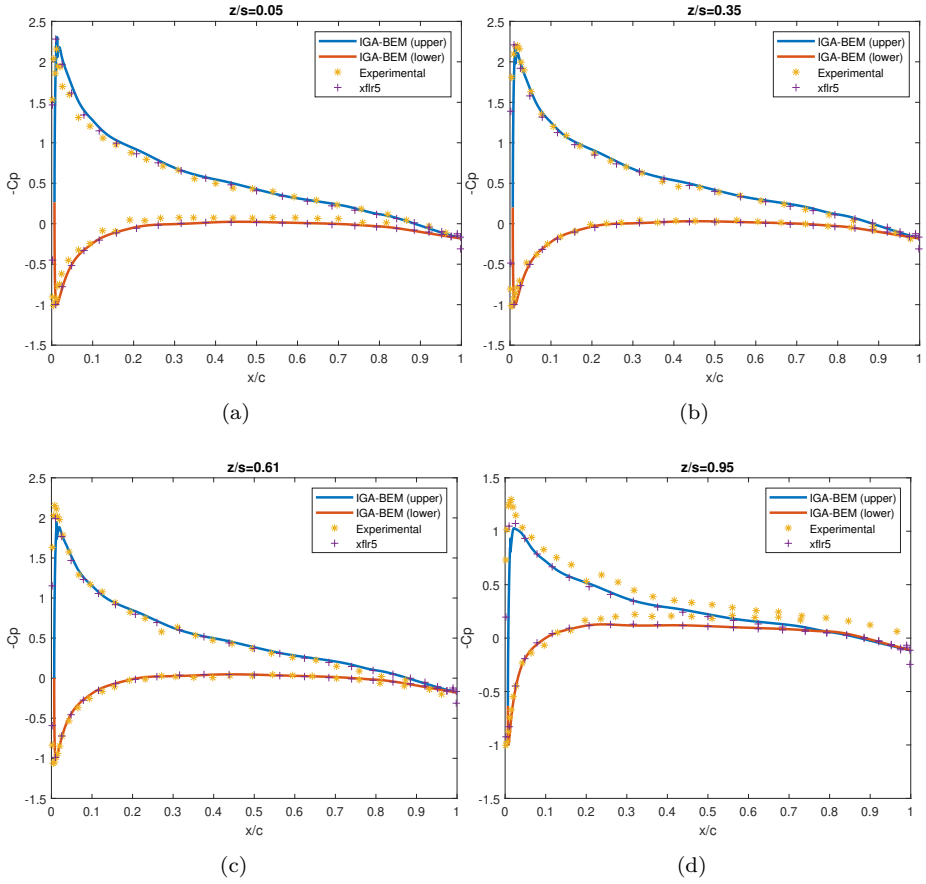

Figure 10: Pressure coefficients for the unswept wing

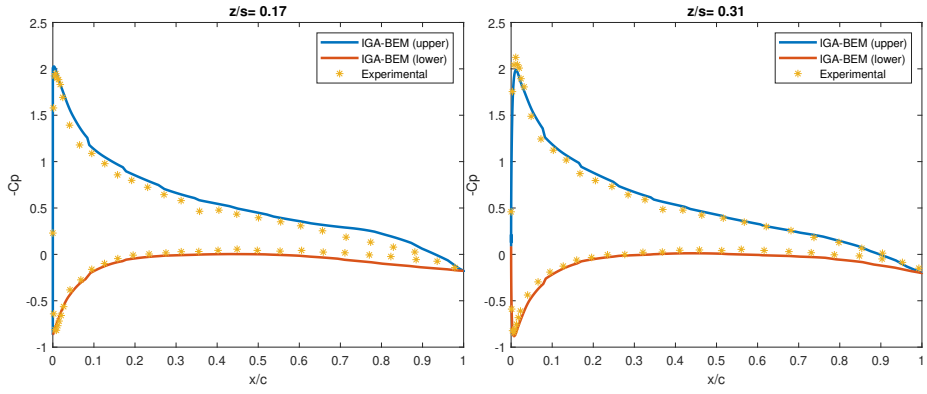

(a)

(b)

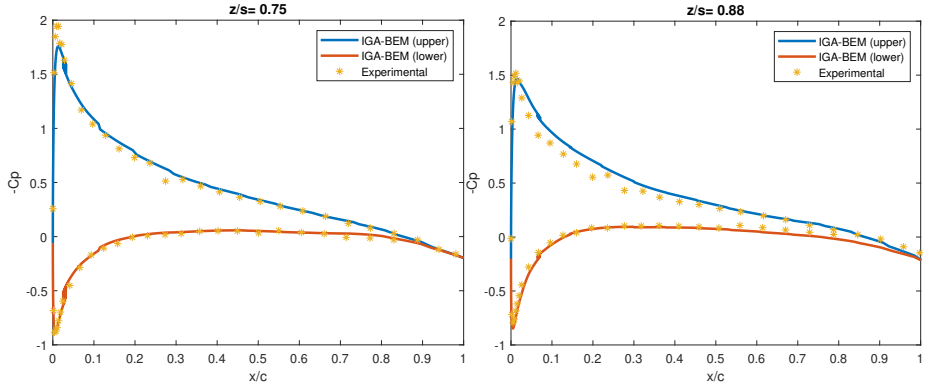

(c)

(d)

Figure 11: Pressure coefficients for the swept wing

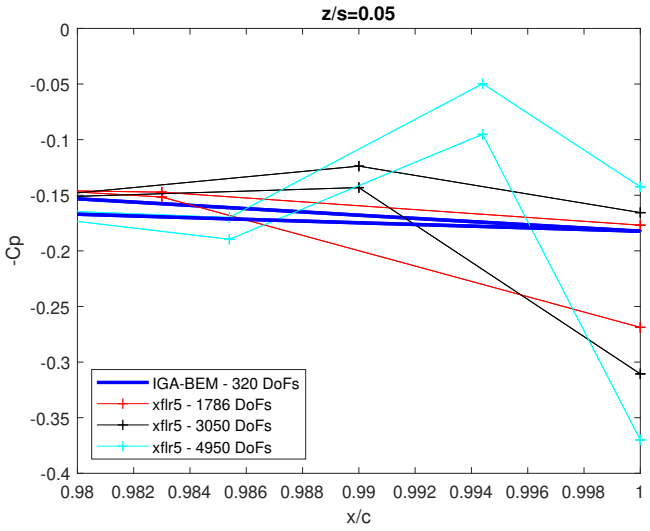

Figure 12: Kutta condition accuracy comparison near the mid section of the unswept wing

4.2. The IGA-based Kutta condition and the flow near the trailing edge

In this subsection we investigate the behaviour of the IGA-based solution of the problem at the trailing edge (TE) and especially near its tip. In this connection, the accuracy and influence of Kutta condition, formulated as a zero pressure-jump condition on the TE (see (17)) and numerically implemented via (18), is assessed and discussed.

Figure 13 depicts the 0^{th}-order iterations, i.e, initial estimations, employed, for different levels of refinement, in the Newton-Raphson scheme used for solving the non-linear system in (18). It is clear from this figure that there is an increasing error in the estimation of the actual zero pressure-jump requirement, especially near the wing tip of the TE, for an increasing number of DoFs. It is also worth noticing that a small but constant error persists along the whole TE. This deviation can be explained by the fact that the initial estimation corresponds to the solution of the non-linear system (18) with the so-called Morino's condition. This condition states that the potential jump on the wake can be approximated by the difference between the potential values on the upper and lower parts of the wing on the TE; see (22). The linear nature of Morino's condition prevents the

0^{th}-order iteration from revealing the observed span-wise cross flow, especially near the tip.

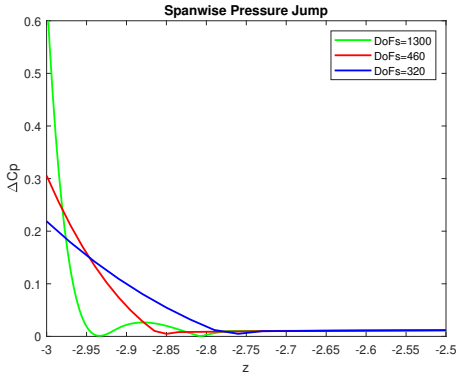

Figure 13: Pressure jump along the trailing edge at the 0^{th} iteration

Figure 13 also indicates that the deviation of the pressure jump from zero becomes more severe as the DoFs of the problem increase. This behaviour is related to the existence of a singularity of the velocity $\nabla\phi$ at the intersection of the trailing edge with the tip, where the flow encounters two sharp edges with dihedral angles greater than π. There has been extensive research in the general field of potential theory as well as in aerodynamic lifting flows for non-smooth domains including sharp edges; see, e.g., [50], [51], and [52], [34]. This analysis concludes that in the vicinity of an edge the gradient of the solution $\phi(\mathbf{P})$ of 3D Laplace equation exhibits the following asymptotic behaviour:

$$\nabla\phi(\mathbf{P}) = O\big(r^{-(1-\pi)/\alpha}\big), \tag{23}$$

where r denotes the Euclidean distance of the field point $\mathbf{P}$ from the edge and α is the magnitude of the exterior of the dihedral angle formed at the edge of the body.

Figure 14 illustrates the configuration for the wing case by taking a plane $\mathcal{P}(x)$, which intersects vertically the wing cap. For the wing geometries considered in this paper (see Fig. 5) it is evident that, as long as the longitudinal coordinate x of $\mathcal{P}(x)$ is different from that of the trailing edge, $\alpha = 3\pi/2$ at both the suction

and the pressure edge of the wing-cap. Then, (23) gives:

$$\nabla\phi(\mathbf{P}) = O(r^{-1/3}),\ x{\neq}\mathrm{TE}_x. \tag{24}$$

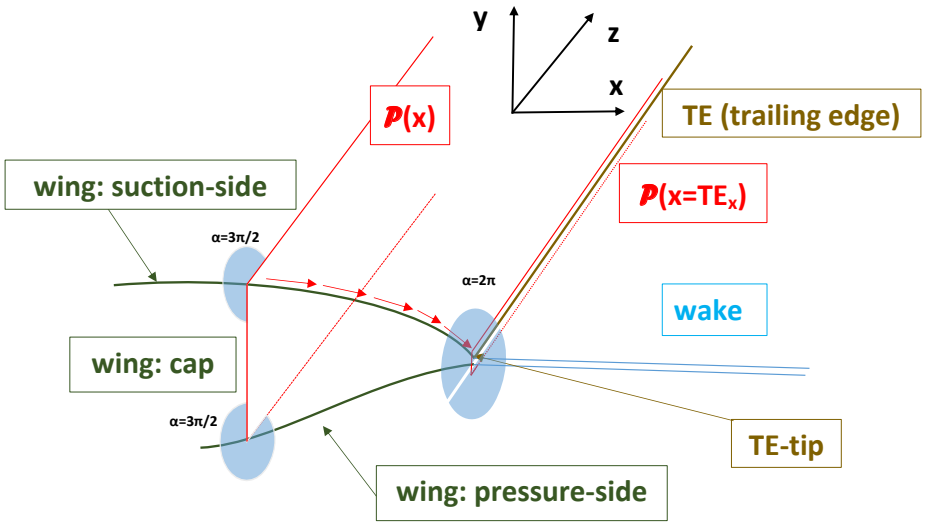

Figure 14: An intersecting plane $\mathcal{P}(x)$ sliding towards the trailing edge TE

However, when $\mathcal{P}(x)$ reaches the trailing edge, $x = \mathrm{TE}_x$, a discontinuity occurs: the two equal dihedral angles at the pressure and suction intersection collapse to a single one equal to $\alpha = 2\pi$, leading to the estimate:

$$\nabla\phi(\mathbf{P}) = O(r^{-1/2}),\ x{=}\mathrm{TE}_x, \tag{25}$$

which indicates that the singularity of the velocity at the TE-tip is stronger than that along the remaining cap-edge.

On the basis of the above discussion it seems legitimate to expect that a higher number of DoFs will have the capacity to reveal the velocity singularity at the tip of TE more accurately. As a result, the error of the initial estimation increases with DoFs, yielding slower convergence in the employed iterative scheme; see Fig. 15.

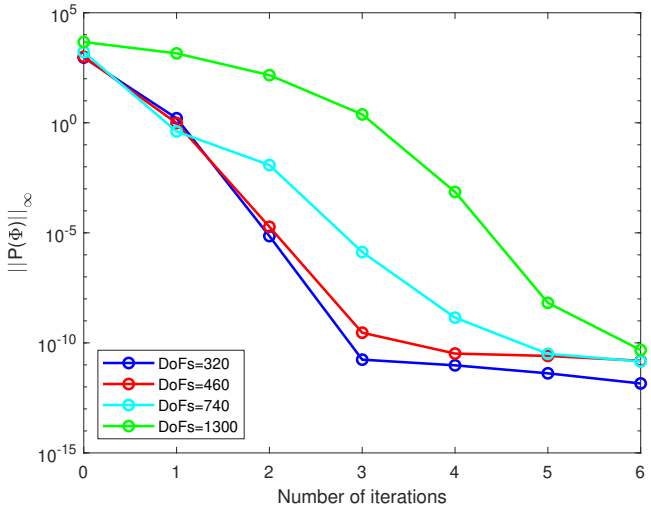

Figure 15: Newton-Raphson scheme convergence for different refinement levels

The effect of tip singularity described in (24) or (25) is of local character, as it is clearly seen in Fig. 13. The local character of the tip singularity is also depicted in Figs. 16 to 19 where the chordwise distribution of C_p at the tip location ($z/s = 1$) and in three sections near the tip ($z/s = 0.99, 0.95, 0.90$) are presented. However, starting from the section at $z/s = 0.95$ and for the remaining wing sections, the initial (0^{th}) and final iterations are almost identical.

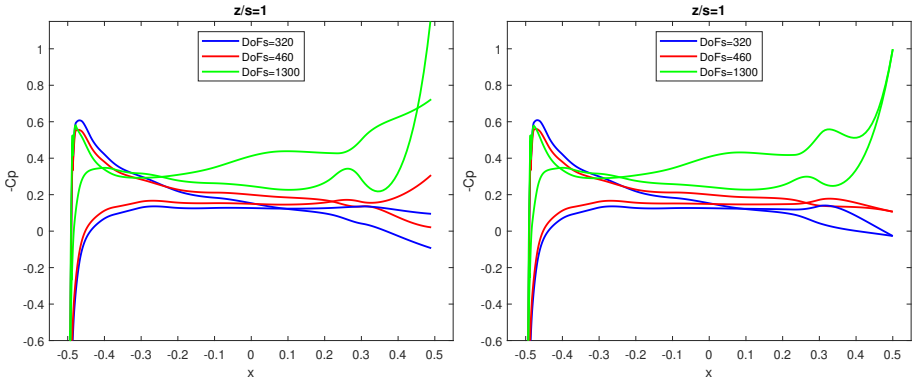

(a) 0^{th}-iteration (Morino) (b) After convergence

Figure 16: Tip chordwise C_p distribution for different refinement levels

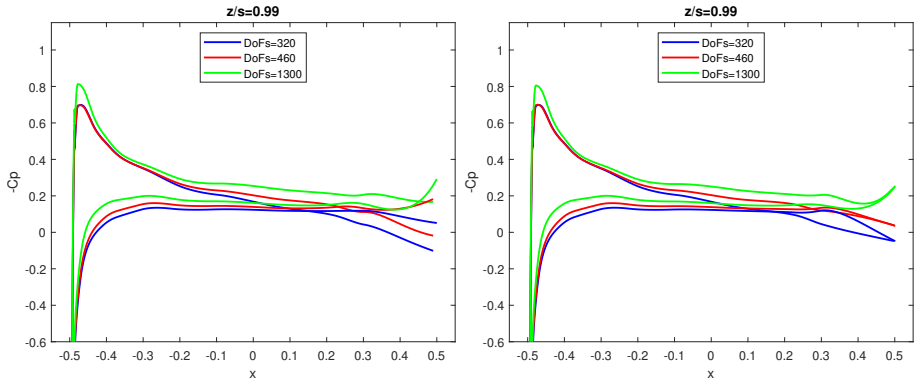

(a) 0^{th} iteration (Morino) (b) After convergence

Figure 17: $z/s = 0.99$ chordwise C_p distribution for different refinement levels

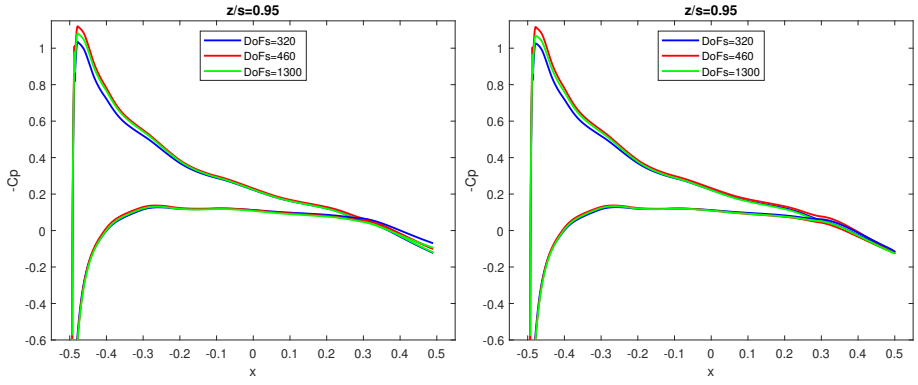

(a) 0^{th} iteration (Morino) (b) After convergence

Figure 18: $z/s = 0.95$ chordwise C_p distribution for different refinement levels

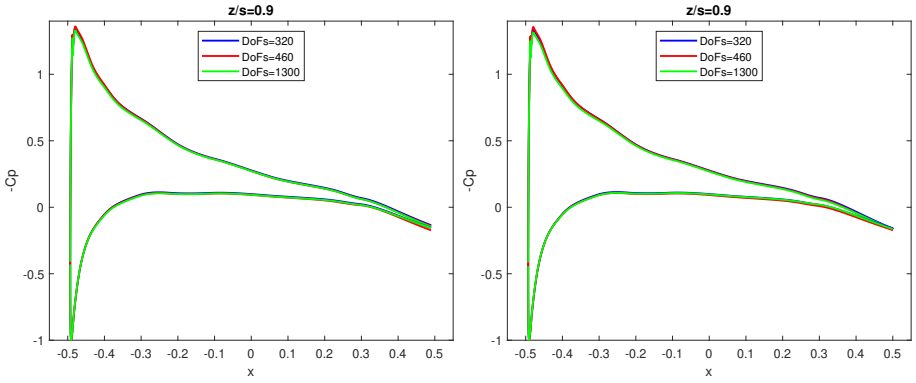

(a) 0^{th}-iteration (Morino) (b) After convergence

Figure 19: $z/s = 0.9$ chordwise C_p distribution for different refinement levels

In the light of the singular character of the solution in the vicinity of the tip, another critical parameter to be assessed for its influence on the accuracy of Kutta condition is the position of the collocation points, especially those near the tip. To assess the performance of Kutta condition we use L^1 and L^∞ norms, defined as:

$$||\Delta cp(\eta)||_{L^1} = \int_{\eta_{mid}}^{\eta_{tip}} \mid \Delta cp(\eta) \mid d\eta \tag{26}$$

$$\|\Delta cp(\eta)\|_{L^\infty} = max\{\Delta cp(\eta), \quad \eta_{tip} \leq \eta \leq \eta_{mid}\} \tag{27}$$

where η_{tip} and η_{mid} are the parametric values of the trailing edge curve that correspond to the tip and mid sections respectively. The wing used for this analysis is the original configuration, shown in Fig. 5a, but with local refinement at the trailing edge region, as shown in Fig. 20. This lets us investigate the behaviour of Kutta condition and, especially, near the tip singularity without introducing redundant DoFs. Some of the benefits of local refinement near singularities in IGA have been demonstrated in [53] where the mesh is refined in the direction of crack propagation.

Results for the pressure jump on the trailing edge are presented when the last

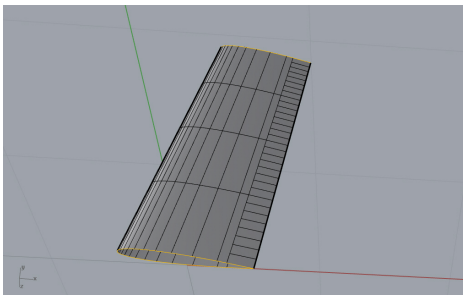

Figure 20: Wing under investigation with TE DoF=35

collocation point is on the tip ($z = -3$) and after shifting it by $0.01, 0.04, 0.07$ and 0.09; see Fig. 21. The rest of the collocation points are also shifted in a way that prevents adjacent ones from being too close to each other, in the sense that the distance between them should not exceed a minimum threshold, while they still remain inside the support of each basis function of the TE curve. The corresponding L^1 and L^∞ norms are presented in Fig. 22. It is clear that, regarding the accuracy of Kutta condition, the best practice is a small shifting of the last collocation point (on the tip); in our case, the best shifting is 0.01. This result remains valid, independently of the level of refinement of the trailing edge region.

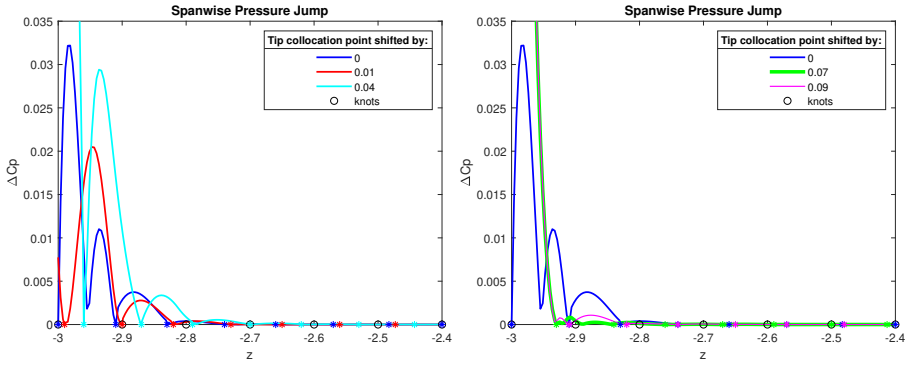

(a) Closest to tip shifted points (b) Further from tip shifted points

Figure 21: Pressure jump on the TE for various positions of the last collocation point. $*$ symbols correspond to positions of collocation points.

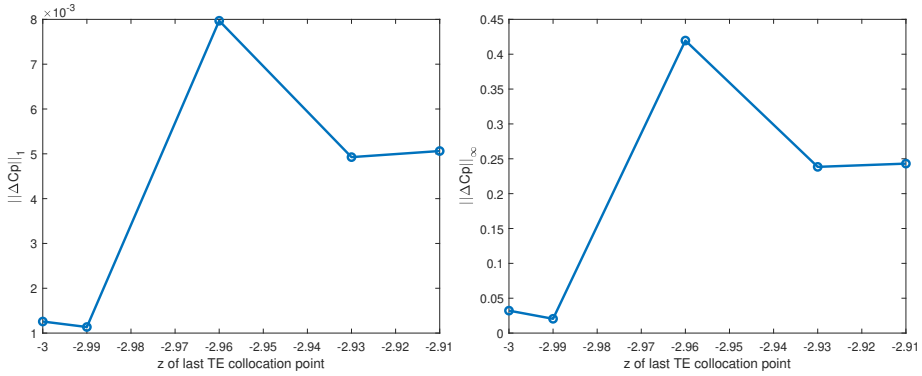

(a) L^1 (b) L^∞

Figure 22: Norms of the pressure jump on the TE for various positions of the last collocation point.

5. Conclusions and future steps

In this work we presented a new Boundary Element Method (BEM) for lifting flows, based on Isogeometric Analysis (IGA). T-splines were used for the representation of all involved geometries and the approximation of the associated field (trace of the velocity potential on the wing). Adopting IGA enables the enforcement of Kutta condition (zero-pressure jump) exactly on the trailing edge (TE) as well as revealing the singular behaviour of the velocity at the TE tip and the wing cap.

The calculated pressure coefficients show good agreement with experiments and superior behaviour when compared to a low order panel method in terms of the required DoFs (Degrees of Freedom) for a given level of accuracy. The implementation of Kutta condition leads to a quadratic system which is solved by an iterative scheme which exhibits fast convergence (5-6 iterations, for all levels of refinement). Furthermore, a numerical investigation is carried out regarding the effect of the tip singularity on Kutta condition for different refinement levels and different locations of the collocation points along the trailing edge. This study reveals that, as the number of DoFs increases, the unboundedness of pressure near the tip becomes evident. Moreover, the zero pressure jump along the trail-

ing edge shows a low L^1 error, especially by slightly shifting the last collocation point from the tip. Note that, since we have opted for T-splines, local refinement has been employed in the trailing edge region in an effort to investigate the behaviour of Kutta condition without introducing redundant DoFs.

This work is based on the assumption of an a-priori known plane wake geometry which serves as a good approximation of lifting flows around bodies placed in uniform streams. The next step is to extend this method to treat more general flows, such as those generated by a rotating propeller of a steadily moving ship. A challenge in this case is that a-priori wake approximations do not work well and it is crucial to develop a wake alignment scheme, that generates a wake geometry on which zero pressure jump is satisfied. This is especially important when the *advance ratio* of the propeller, namely the ratio of the ship speed over the propeller's rotational speed, is quite low which imply that one of the blades could operate within the flow of the wake of another blade, as stated for example in [11].

Acknowledgements

This work has received funding from the European Union's Horizon 2020 research and innovation programme under the Marie Skłodowska-Curie grant *"ARCADES: Algebraic Representations in Computer-Aided Design for complEx Shapes"* (agreement No. 675789) and from the Nazarbayev University under the grant: *"SOLTIGA: Shape Optimization of Lift- and Thrust-generating surfaces with the aid of IsoGeometric Analysis"* (grant award No. 090118FD5328).

References

[1] L. Morino, C. Kuo, Subsonic potential aerodynamics for complex configurations: A general theory, AIAA journal 12 (1974).

[2] H. Ashley, S. Widnall , M.T. Landahl, New Directions in Lifting Surface Theory, AIAA Journal 3 (1965) 3–16.

[3] M.T. Landahl, V.J.E. Stark, Numerical Lifting-Surface Theory - Problems and Progress, AIAA Journal, 3 (1968) 2049–2060.

[4] N.T. Frink, S.Z. Pirzadeh, P.C Parikh, M.J. Pandya, M.K. Bhat, The NASA tetrahedral unstructured software system (TetrUSS), The Aeronautical Journal 104 (2000) 491–499.

[5] M. Abdel-Maksoud, H.-J Heinke, Scale effects on ducted propellers, Proceedings, The 24th Symposium on Naval Hydrodynamics, July 8–13, Fukuoka, Japan (2002).

[6] J. Hess, A.M.O. Smith, Calculation of non-lifting potential flow about arbitrary three-dimensional bodies, Journal of Ship Research 8 (1964).

[7] J.L. Hess, Calculation of Potential Flow about Arbitrary Three-Dimensional Bodies, Report No. MDC J5679-01 (1972).

[8] J.T. Lee, A Potential Based Panel Method for the Analysis of Marine Propellers in Steady Flow , PhD Thesis, Department of Ocean Engineering, MIT (1987).

[9] J.E. Kerwin, S.A. Kinnas, J. Lee, W. Shih, A Surface Panel Method for the Hydrodynamic Analysis of Ducted Propellers, TRANS. SNAME 95 (1987).

[10] G.-D. Kim, C.-S. Lee, J.E. Kerwin, A B-spline based higher order panel method for analysis of steady flow around marine propellers, Ocean Engineering 34 (2007) 2045–2060.

[11] Y. Tian, S.A. Kinnas, A wake model for the prediction of propeller performance at low advance ratios, Int J Rotating Mach 2012 (2012) 1–11.

[12] G.-D. Kim, B.-K. Ahn, J.-H. Kim, C.-S. Lee, Improved Hydrodynamic Analysis of Marine Propellers Using a B-Spline-Based Higher-Order Panel Method, J Mar Sci Technol 20:670 to 678 (2015).

[13] Y. Wang, M. Abdel-Maksoud, B. Song, Convergence of different wake alignment methods in a panel code for steady-state flows, Journal of Marine Science and Technology 21 (2016) 567–578.

[14] Y. Wang, M. Abdel-Maksoud, B. Song, A fast method to realize the pressure Kutta condition in boundary element method for lifting bodies, Ocean Engineering 130 (2017) 398–406.

[15] Y. Wang, M. Abdel-Maksoud, Coupling wake alignment lifting line method and boundary element method for open water and unsteady propeller simulation, Ocean Engineering 213 (2020) 107738.

[16] T.J.R. Hughes, J.A. Cottrell, Y. Bazilevs, Isogeometric analysis: CAD, finite elements, NURBS, exact geometry and mesh refinement, Comput. Methods Appl. Mech. Engrg. 194 (2005) 4135–4195.

[17] J.A. Cottrell, T.J.R. Hughes, Y. Bazilevs, Isogeometric Analysis: Toward Integration of CAD and FEA, Wiley, Chichester (2009).

[18] J.A. Cottrell, A. Reali, Y. Bazilevs, Isogeometric analysis of structural vibrations, Comput. Methods Appl. Mech. Engrg. 195 (2006) 5257–5296.

[19] K.A. Belibassakis, Th.P. Gerostathis, K.V. Kostas, C.G. Politis, P.D. Kaklis, A.I. Ginnis, C. Feurer, A BEM-isogeometric method for the ship wave-resistance problem, Ocean Engineering 60 (2013) 53–67.

[20] P. D. Kaklis, C. G. Politis, K. A. Belibassakis, A. I. Ginnis, K. V. Kostas, G. P. Gerostathis, Encyclopedia of Computational Mechanics Second Edition, Vol. Fluids–Part 2, Wiley, 2017, Ch. Boundary-Element Methods and Wave Loading on Ships, pp. 1–35.

[21] C.G. Politis, A. Papagiannopoulos, K.A. Belibassakis, P.D. Kaklis, K.V. Kostas, A.I. Ginnis, T.P. Gerostathis, An Isogeometric BEM for Exterior Potential-Flow Problems Around Lifting Bodies, Proceedings, 11th World Congress on Computational Mechanics (WCCM XI) (2014).

[22] M.A. Scott, R.N. Simpson, J.A. Evans, S. Lipton, S.P.A. Bordas, T.J.R. Hughes, T.W. Sederberg, Isogeometric boundary element analysis using unstructured T-splines, Comput. Method Appl. Mech. Engrg. 254 (2013) 197–221.

[23] K. Kostas, M. Fyrillas, C. Politis, A. Ginnis, P. Kaklis, Shape optimization of conductive-media interfaces using an IGA-BEM solver, Computer Methods in Applied Mechanics and Engineering 340 (2018) 600 – 614. doi:https://doi.org/10.1016/j.cma.2018.06.019.

[24] Z. Liu, M. Majeed, F. Cirak, R.N. Simpson, Isogeometric FEM-BEM coupled structural-acoustic analysis of shells using subdivision surfaces, International Journal for Numerical Methods in Engineering 00 (2016) 1–29.

[25] L. Piegl, W. Tiller, The NURBS Book, Springer Verlag (1997).

[26] D. Forsey, R. Bartels, Hierarchical B-Spline Refinement, SIGGRAPH: Proceedings of the 15th annual conference on Computer graphics and interactive techniques (1988) 205–212.

[27] T. Dokken, T. Lyche, K. Pettersen, Polynomial splines over locally refined box-partitions, Computer Aided Geometric Design 30 (2013) 331–356.

[28] T.W. Sederberg, J. Zheng, A. Bakenov, A. Nasri, T-splines and T-NURCCs, ACM Transactions on Graphics 22 (2003) 477–484.

[29] Y. Bazilevs, V.M. Calo, J.A. Cottrell, J.A. Evans, T.J.R. Hughes, S. Lipton, M.A. Scott, T.W. Sederberg, Isogeometric analysis using T-splines, Comput. Methods Appl. Mech. Engrg. 199(5-8) (2010) 229–263.

[30] E. Atroshchenko, S. Tomar, G. Xu , S.P.A Bordas, Weakening the tight coupling between geometry and simulation in isogeometric analysis: from sub-and super-geometric analysis to Geometry Independent Field approximaTion (GIFT), International Journal for Numerical Methods in Engineering 114 (2018) 1131–1159.

[31] X. Li, J. Zheng, T.W. Sederberg, T.J.R Hughes, M.A. Scott, On Linear Independence of T-spline Blending Functions, Computer Aided Geometric Design 29 (2012) 63–76.

[32] S.P. Chouliaras, An Isogeometric Boundary Element Method for Three-Dimensional Lifting Flows, Doctoral dissertation, University of Strathclyde, Glasgow, United Kingdom (2020).

[33] J. Newman, Marine hydrodynamics, MIT Press (1977).

[34] L. Morino, G. Bernardini, Singularities in BIEs for the Laplace equation; Joukowski trailing-edge conjecture revisited, Engineering Analysis with Boundary Elements 25 (2001) 805–818.

[35] J.E. Kerwin, J.B. Hadler, The principles of naval architecture: Propulsion, The Society of Naval Architects and Marine Engineers (2010).

[36] A.I. Ginnis, K.V. Kostas, C.G. Politis, P.D. Kaklis, K.A. Belibassakis, Th.P. Gerostathis, M.A. Scott, T.J.R. Hughes, Isogeometric boundary-element analysis for the wave-resistance problem using T-splines, Comput. Methods Appl. Mech. Engrg. 279 (2014) 425–439.

[37] R. Sharma, T.-W. Kim, R. Lee Storch, H. J. Hopman, S. O. Erikstad, Challenges in computer applications for ship and floating structure design and analysis, CAD 44 (2012) 166–185.

[38] K.V. Kostas, A.I. Ginnis, C.G. Politis, P.D. Kaklis, Ship-hull shape optimization with a T-spline based BEM-isogeometric solver, Comput. Methods Appl. Mech. Engrg. 284 (2015) 611–622.

[39] A. Arapakopoulos, R. Polichshuk, Z. Segizbayev, S. Ospanov, A. Ginnis, K. Kostas, Parametric models for marine propellers, Ocean Engineering 192 (2019) 106595. doi:https://doi.org/10.1016/j.oceaneng.2019.106595.
URL http://www.sciencedirect.com/science/article/pii/S002980181930719X

[40] T. S. Zheng,, X. Song, Knot intervals and multi-degree splines, Comput. Aided Geom. Design 20 (2003) 455–468.

[41] T.W. Sederberg, D.L. Cardon, G.T. Finnigan, N.S. North, J., Zheng, T., Lyche, T-spline simplification and local refinement, ACM Trans. Graph. 23 (2004) 276–283.

[42] M. A. Scott, M. J. Borden, C. V. Verhoosel, T. W. Sederberg, T. J. R. Hughes, Isogeometric finite element data structures based on Bézier extraction of T-splines, International Journal for Numerical Methods in Engineering 88 (2) (2011) 126–156.

[43] M. Scott, X. Li, T. Sederberg, T. Hughes, Local refinement of analysis-suitable T-splines, Comput. Methods Appl. Mech. Engrg. 213-216 (2012) 206 – 222.

[44] L. Morino, A general theory of unsteady compressible potential aerodynamics, NASA-CR-2464 (1974).

[45] J.F.C Telles, A self-adaptive co-ordinate transformation for efficient numerical evaluation of general boundary element integrals, Int. J. Numer. Methods.Eng. 24, 959–973 (1987).

[46] J.F.C Telles, R.F. Oliveira, Third degree polynomial transformation for boundary element integrals: further improvements, Eng. Anal. Boundary Elem. 13, 135–141 (1994).

[47] K. Kostas, A. Amiralin, S. Sagimbayev, T. Massalov, Y. Kalel, C. Politis, Parametric model for the reconstruction and representation of hydrofoils and airfoils, Ocean Engineering 199 (2020) 107020. doi:https://doi.org/10.1016/j.oceaneng.2020.107020.

[48] L.P. Yip, G.L Shubert, Pressure Distributions on a 1- by 3-Meter Semispan Wing at Sweep Angles From 0° to 40° in Subsonic Flow, NASA TN D-8307 (1976).

[49] W. Geissler, Nonlinear Unsteady Potential Flow Calculations for Three-Dimensional Oscillating Wings, AIAA Journal 16 (1978).

[50] V.A. Kondrat'ev, O.A. Oleinik, Boundary-value problems for partial differential equations in non-smooth domains, Russian Mathematical Surveys 38 (1983) 3–76.

[51] D. Lesnic, L. Elliott, D.B. Ingham, Treatment of singularities in exterior fluid domains with corners using the boundary element method, Computers and Fluids 23 (1994) 817–827.

[52] J.L. Hess, Review of integral-equation techniques for solving potential flow problems with emphasis on the surface source method, Comput. Methods Appl. Mech. Engrg. 5 (1975) 145–196.

[53] X. Peng,E. Atroshchenko, P. Kerfriden, S.P.A Bordas, Isogeometric boundary element methods for three dimensional static fracture and fatigue crack growth, Comput. Methods Appl. Mech. Engrg. 316 (2017) 151–185.